Atomic-scale scanning of domain network in the ferroelectric HfO_2 thin film

Kunwoo Park[1,2†], Dongmin Kim[1,2,3†], Kyoungjun Lee[4], Hyun-Jae Lee[5], Jihoon Kim[1,2], Sungsu Kang[1,2], Alex Lin[6], Alexander James Pattison[6], Wolfgang Theis[7], Chang Hoon Kim[5], Hyesung Choi[1,2], Jung Woo Cho[4], Peter Ercius[6], Jun Hee Lee[5]*, Seung Chul Chae[4]* and Jungwon Park[1,2,8,9]**

[1]Center for Nanoparticle Research, Institute for Basic Science (IBS), Seoul 08826, Republic of Korea

[2]School of Chemical and Biological Engineering, Institute of Chemical Process, Seoul National University, Seoul 08826, Republic of Korea

[3]Samsung Advanced Institute of Technology, Samsung Electronics, Suwon-si, Gyeonggi-do 16678, Republic of Korea

[4]Department of Physics Education, Seoul National University, Seoul 08826, Republic of Korea

[5]Department of Energy Engineering, School of Energy and Chemical Engineering, Ulsan National Institute of Science and Technology (UNIST), Ulsan 44919, Republic of Korea

[6]National Center for Electron Microscopy, Molecular Foundry, Lawrence Berkeley National Laboratory, Berkeley, CA 94720, USA

[7]Nanoscale Physics Research Laboratory, School of Physics and Astronomy, University of Birmingham, Birmingham B15 2TT, UK

[8]Institute of Engineering Research, College of Engineering, Seoul National University, Seoul 08826, Republic of Korea

[9]Advanced Institute of Convergence Technology, Seoul National University, Suwon-si, Gyeonggi-do 16229, Republic of Korea

† K.P. and D.K. contributed equally to this work.

* These authors jointly supervised this work: P. Ercius (percius@lbl.gov), J. H. Lee (junhee@unist.ac.kr), S. C. Chae (scchae@snu.ac.kr), and J. Park (jungwonpark@snu.ac.kr)

ABSTRACT

Ferroelectric HfO_2-based thin films have attracted much interest in the utilization of ferroelectricity at the nanoscale for next-generation electronic devices. However, the structural origin and stabilization mechanism of the ferroelectric phase are not understood because the film is typically nanocrystalline with active yet stochastic ferroelectric domains. Here, electron microscopy is used to map the in-plane domain network structures of epitaxially grown ferroelectric Y:HfO_2 films in atomic resolution. The ferroelectricity is confirmed in free-standing Y:HfO_2 films, allowing for investigating structural origin for their ferroelectricity by 4D-STEM, high-resolution STEM, and iDPC STEM. At the grain boundaries of <111>-oriented $Pca2_1$ orthorhombic grains, a high-symmetry mixed-(R3m, $Pnm2_1$) phase is induced, exhibiting enhanced polarization due to in-plane compressive strain. Nanoscale $Pca2_1$ orthorhombic grains and their grain boundaries with mixed-(R3m, $Pnm2_1$) phases of higher symmetry cooperatively determine the ferroelectricity of the Y:HfO_2 film. It is also found that such ferroelectric domain networks emerge when the film thickness is beyond the finite value. Furthermore, in-plane mapping of oxygen positions overlaid on ferroelectric domains discloses that polarization is suppressed at vertical domain walls while it is active when domains are aligned horizontally with sub-angstrom domain walls. In addition, randomly distributed 180˚ charged domain walls are confined by spacer layers.

KEYWORDS: Ferroelectricity, HfO_2, grain boundaries, crystal structure, domain network

INTRODUCTION

The discovery of ferroelectric HfO_2 thin films in 2011 has led to great attention due to its coercive field, scalability down to sub-10 nm scale, and compatibility with conventional silicon-based device engineering.[1] Spontaneous polarization of ferroelectrics offers the promise of nonvolatile memory applications, potentially reducing energy consumption through the elimination of the need for constant power to maintain data.[2–7] These attractive properties allow the utilization of ferroelectric films in various next-generation electronic devices such as nonvolatile memories, negative capacitance field-effect transistors, and neuromorphic synaptic devices.[8–10]

The first observation of the polar non-centrosymmetric $Pca2_1$ orthorhombic phase (o-phase) and related spontaneous polarization in HfO_2 thin films was reported.[1] This phase is widely accepted as the structural origin of the ferroelectricity in HfO_2-based thin films;[1,11] however, the existence of the o-phase is not justified by the bulk phase diagram of HfO_2.[12] The stable phase of bulk HfO_2 at standard temperature and pressure is the $P2_1/c$ monoclinic phase (m-phase), which can be transformed into the $P4_2/nmc$ tetragonal phase (t-phase) and the Fm-3m cubic phase (c-phase) at 1973 and 2773 K, respectively.[9] It has been observed that the metastable o-phase is possibly stabilized under certain conditions affected by doping, film thickness, and local strain effects.[1,13,14] HfO_2 films, generally when nanocrystalline, exhibit ferroelectricity. Recent studies have also demonstrated the observation of ferroelectricity in bulk hafnia.[15,16] Furthermore, ferroelectric HfO_2 films exhibit a wake-up effect, characterized by changes in remnant polarization after multiple switching cycles. This phenomenon can be attributed to various causes, such as the activation of initially inactive ferroelectric domains, intensifying local domains, defects, or local strain variations. Thus, to understand the stabilization mechanism and the controlled formation of the ferroelectric o-phase, insights into the structure of the ferroelectric HfO_2 film are needed. Indeed, there are open questions

regarding how the size, structure, and distribution of domains within the film, and the structure of grain boundaries impact on the macroscopic ferroelectric properties. Knowing how atomic structural characteristics lead to the ferroelectricity of HfO_2 thin films would define the size limit for the existence of a homogeneous ferroelectric phase throughout the entire film.

Directly characterizing the grain structure and the ferroelectric domain is challenging even using state-of-the-art experimental techniques. X-ray diffraction is a conventional structure analysis platform for thin-film materials but has limitations in studying ferroelectric HfO_2. Distinguishing different phases of HfO_2 is not trivial since the o-phase exhibits an almost identical atomic structure to the t-phase.[1,11,17,18] Moreover, the R3m rhombohedral phase (r-phase), which is a recently reported ferroelectric phase, also has a similar structure to the aforementioned o- and t-phases.[19] It has been recently reported that the intercalation of Hf atoms stabilizes the r-phase and results in an ultralow coercive field.[20] Phase distinction becomes more difficult as the film thickness approaches the nanoscale since the diffraction peaks are broadened following the Scherrer equation.[21,22] Cross-sectional (scanning) transmission electron microscopy ((S)TEM) has also been used to investigate such phases, but accessible crystallographic information is limited to a few domains which align along a particular zone axis in a vertical cross-section.[18] In addition, the determination of oxygen atom positions across a wide area, which is necessary for ferroelectric domain mapping, is exceptionally difficult due to their weak scattering.[23]

In this work, we synthesize free-standing ferroelectric Y:HfO_2 films and study them with advanced (S)TEM techniques coupled with simulations. Correlated nano-scale four-dimensional scanning transmission electron microscopy (4D-STEM) and micrometer-scale atomic-resolution STEM (AR-STEM) show that a high symmetry phase, which is compressively strained along the in-plane direction, is surprisingly located at boundaries between ferroelectric o-phase grains in (111)-oriented films. We conduct first-principles

calculations based on density functional theory (DFT) to interrogate the phonon modes in the domain network structures. The calculations reveal that the phonon coupling induces a large polarization in the polar mixed-(R3m, $Pnm2_1$) phase that increases by the out-of-plane tensile strain. These combined experimental and theoretical results indicate that the interaction between grains leads to the formation of a ferroelectric phase, which should be considered an important factor for understanding the ferroelectricity of HfO_2 thin films. Also, in-plane atomic-scale (S)TEM observations of films with different thicknesses from 1.5 to 11 nm confirm that the film with a 1.5 nm thickness is composed of the t-phase, while 5.5 nm and 11 nm thick films dominantly consist of the o-phase. Moreover, in-plane integrated differential phase contrast-STEM (iDPC-STEM) enables displacement mapping of oxygen atoms across many domains, which directly reveals the characteristic ferroelectric domain walls[24] and domain distribution within (100)-oriented HfO_2 thin films. The non-polar phase regions are observed at vertical domain walls, and DFT calculations show that suppression of polarization can occur where the domains are attached vertically. In addition, randomly distributed 180 ° charged domain walls are observed to be confined by spacer layers.

RESULT AND DISCUSSION

Free-standing Ferroelectric Y:HfO_2 Thin Films

We prepared free-standing Y:HfO_2 films for micrometer-scale in-plane observation of epitaxial Y:HfO_2 films, as described in a schematic diagram in Figure 1a. Epitaxial $La_{0.7}Sr_{0.3}MnO_3$ (LSMO) was grown on a $SrTiO_3$ (STO) substrate as a sacrificial layer. A Y:HfO_2 film with <111> out-of-plane direction and controlled thickness was grown on the LSMO (see Methods). The LSMO layer was removed by a selective wet-etching process with an aqueous solution of KI and HCl.[25,26] The detached polymer-supported free-standing Y:HfO_2 films were transferred to TEM grids (holey carbon grids, holey silicon nitride grids, etc.) for in-plane

imaging or other substrates for electronic measurement.

Large free-standing areas of Y:HfO_2 film stay intact across the TEM grid as confirmed by optical microscopy and TEM imaging (Figure 1b). High magnification TEM images reveal the configuration of grains and their atomic structure within the film. Conversely, a close examination of the cross-sectional STEM images for films with thicknesses of 11 nm, 5.5 nm, and 1.5 nm, which are extensively analyzed in the subsequent sections, reveals overlapping grains and a restricted viewing area, as illustrated in Figures 1c, 1d, and 1e. Furthermore, it becomes evident that the zone axes in the cross-sectional perspective are not ideally suited for phase analysis, a topic that will be expanded upon in the following section via STEM simulation and magnified images. To prove that the ferroelectricity of the as-grown film (before PMMA spin-coating) is maintained after the transfer process, we measured the polarization switching behavior of the Y:HfO_2 films (Figure S1). The polarization-voltage (P-V) loops of as-grown and transferred films show that the remnant polarization increases with decreasing thickness and is enhanced after the transfer process, which can be attributed to the release of strain and the substrate effect.[19,27]

The free-standing Y:HfO_2 film exposes in-plane structures over a millimeter-scale region. We studied the film using 4D-STEM and automated large-area AR-STEM imaging in the same region (Figure 2a) with aberration-corrected STEM (Cs-corrected-STEM). In 4D-STEM, a nearly-parallel beam of electrons is rastered across the sample in a two-dimensional grid and a nanobeam diffraction (NBD) pattern is acquired at each position. Each pattern provides a local measurement of the material phase with nanometer-scale resolution.[28–30] The diffraction intensity of spots corresponding to different HfO_2 phases is then integrated in every pattern, generating a real-space virtual dark field (VDF) image that shows crystallographic phase maps over a large area. Subsequently, atomic-resolution high-angle annual dark-field (HAADF)-STEM images are acquired using an automated routine over regions that span several hundreds

of nanometers.[31] Typical HAADF-STEM images with sub-Angstrom resolution can only be acquired over a field of view of < 50nm. A custom automated routine was used to acquire a grid of 7×7 images of the same ~350 nm region scanned by 4D-STEM, significantly increasing the number of observed grains. Such correlative real-space and diffraction space information of the same region from NBD, 4D-STEM, and automated AR-STEM enables the comparison of the local atomic arrangement in different phases and the characterization of each phase, as shown in Figures 2b, 2c. The VDF image from the 4D-STEM scan shows that phase differences between grain boundaries and cores exist throughout a large area of the free-standing Y:HfO_2 film, as seen in Figures 2d, 2e. The 7×7 automated AR-STEM images for the corresponding region are placed on a low-magnification STEM image (yellow boxes) in Figure 2b. Each image offers a clear view of the grain boundaries and atomic structure (Figures 2f, 2g).

Inducement of Strained Polar Phase at Grain Boundaries

The ferroelectricity of the entire HfO_2 film is produced by the collective contribution of individual active nanograins interconnected by grain boundaries. To uncover how the ferroelectricity of the HfO_2 thin film is affected by the crystallographic phase distribution and grain configuration, we performed correlative 4D-STEM and automated AR-STEM analysis on the 11 nm thick Y:HfO_2 thin film, which shows strong ferroelectricity (Figure S1). Relatively low symmetry in the o-phase enables its distinction from the phase with high symmetry (HS-phase) since several lattice reflections in the HS-phase are forbidden[32] and multiple scattering is negligible in such a thin film for 300 kV electrons. The mean diffraction pattern summed from all probe positions is shown in Figure **3**a. There are two sets of interesting diffraction spots which can be used to delineate the o- and HS-phases[32]. Spots marked with red circles (called virtual detector 1) are indicative of both phases, and diffraction spots marked with orange circles (called virtual detector 2) are allowed for the o-phase but are forbidden for the HS-phase. The

corresponding VDF images formed by summing the intensities in virtual detectors 1 and 2 exhibit different morphology in the distribution of crystallographic phases. The simulated CBED images for four different crystallographic phases of $Pca2_1$ o-phase, $Pnm2_1$ o-phase, R3m r-phase, and $P4_2/nmc$ t-phase along the [111] orientation are shown in Figure S2. The VDF images from detector 2 show o-phase grains in high contrast and HS-phase regions in low contrast (Figure 3c, and Figure S5). In the VDF images from detector 1, both the o-phase and HS-phase exhibit high contrast (Figure 3b, and Figure S4). The signals in the VDF images could be influenced by the distribution of phases as well as other factors of the thin film materials. For example, in thin film materials, it is common to have grain boundaries with intrinsically low atomic density, pores induced from lattice mismatch, and deviation from zone axes. However, those other factors are consistent for both VDF images from virtual detectors 1 and 2, validating the contrast difference between the two images is mainly from the difference in phase (Figure S6). Interestingly, some grain boundaries identified by AR-STEM, where the grains attach to each other with 60 or 120 degrees, are distinguishable by low contrast of HS-phase in the detector 2. This contrast difference at grain boundaries indicates that grain boundaries between o-phase grains have HS-phase. The automated AR-STEM image for the corresponding region shows the location of grain boundaries and the direction in which the grains are attached (Figure 3d, and Figiure S6). 4D-STEM and AR-STEM images for the representative regions with grain boundaries which show high contrast in detector 1 and low contrast in detector 2 are displayed in Figure 3e and Figure S8 (see Text S1). This morphology is representative of the micrometer scale area, as seen in Figure 3b to 3e, and Figures S2 to S7, which demonstrates that the portion of the HS-phase, mainly located along the grain boundaries between o-phase grains, is large, which can potentially affect the overall ferroelectricity of the entire film.

Further AR-STEM was conducted on specific regions of interest of an 11 nm thick free-standing Y:HfO_2 film to support the findings of the emergence of the HS-phase near the grain boundaries discovered by 4D-STEM and automated AR-STEM. Grains with the o-phase located in the center were confirmed by the simulated STEM images and atomic models of conventionally known ferroelectric o-phase in the [111] direction (Figure 4a). Additionally, such epitaxial growth was also confirmed in the cross-sectional STEM images (Figure S10e). This result indicates that nanoscale domains possessing the o-phase form an in-plane network, serving as an important contributor for the ferroelectricity of the overall film.

Notably, the atomic structure becomes symmetric near the grain boundary, consistent with 4D-STEM observations. This is interpreted as the formation of the HS-phase rather than the o-phase. In the [111] viewing direction, the atomic distance of the o-phase alternates between short and long distances, as demonstrated in the simulated image (Figure 4a) and the measured intensity profile (Figure 4c). In contrast to the o-phase, the distances between atoms are constant at the boundaries as shown in the AR-STEM image and intensity profile in Figure 4c. Moreover, the atomic distances noticeably decrease at the grain boundaries. Strain maps from geometric phase analysis (GPA) and real-space phase analysis both show that the large compressive strain is perpendicularly applied to the grain boundaries (Figure 4b and see Methods). Strain maps for another direction and the direction of the compressive strain are shown in Figure S9. Increased compressive strain at grain boundaries in thin films has been reported in many thin-film systems.[33,34] Deposition flux can induce adatoms on the surface, which are attracted to the boundaries where the chemical potential energy is low.[35] As a result, the atomic distances shrink and compressive strain at grain boundaries is generated.[35] These phenomena are likely to occur in the nanometer-thick HfO_2 thin films we study here, as they were synthesized by a similar deposition process as reported elsewhere (see Methods).

It is worth noting that crystallographic identification for the ferroelectric domain and grain boundaries, explained above, became possible with the in-plane analysis. Such studies are very limited in conventional cross-sectional analysis. Nonetheless, cross-sectional AR-STEM analysis has been performed for comparison (Figure S10). Unlike the in-plane analysis, cross-sectional images suffer from several problems such as overlapping features at grain boundaries non-orthogonal to the viewing direction and the inability to distinguish similar atomic arrangements corresponding to many different zone axes. With a grain size of around 10 nm, it is difficult to avoid overlapped information in cross-sectional TEM samples. In addition, the atomic arrangements in potential zone axes for cross-sectional views (<1-10>, <10-1>, <01-1>, <11-2>, <1-21>, and <-211>) are almost identical in the o-phase and the high symmetric phase, except for the <11-2> direction (Figure S11), which is not the case for the in-plane viewing direction (<111>).

As the occupancy of the HS-phase and the applied strain along the boundaries are substantial, it is important to understand their effect on ferroelectricity. We conducted first-principles calculations based on DFT (Text S1 and Figure S12). The situation where two <111> oriented o-phase domains are attached at an angle of 120 degrees is represented by the atomic model in Figure 4d. Relaxation at the interdomain area triggers phonon coupling that induces a polar mixed-(R3m, $Pnm2_1$) phase with higher symmetry than the o-phase, which is consistent with the experimental HR-STEM data. The mixed-(R3m, $Pnm2_1$) phase possesses induced phonon modes including $X_2', Y_2', Z_2', X_1, Y_1, Z_1, \Gamma_{15}^x, \Gamma_{15}^y, \Gamma_{15}^z, \Gamma_{25}^z, Z_5^x$ and Z_5^y phonons. Importantly, among those phonons, $\Gamma_{15}^x, \Gamma_{15}^y$, and Γ_{15}^z phonons create a uniform polarization for R3m phase in the <111> direction with all oxygen atoms shifting along the x, y, and z axes respectively. For the $Pnm2_1$ phase, Γ_{15}^x and Γ_{15}^y phonons contribute to the <110> directional polarization. Calculations involving inner-atomic relaxation, assuming that the HS-phase is securely anchored between the two grains, reveal that the amplitudes of modes constituting $Pnm2_1$ are

relatively smaller than those for R3m. Conversely, a full relaxation calculation that considers the strain effect demonstrates that the phonon modes comprising $Pnm2_1$ are amplified in comparison to the amplitudes found in the inner-atomic relaxation (Figure S13). It is worth noting that the induced phase presents about 16 times stronger polarization than the previously reported r-phase under no strain.[19] All the phonon modes are designated based on irreducible representations in relation to the high-symmetry cubic phase (Fm-3m).

Additionally, we calculated the crystal structures and interface energies after arranging various phases at the grain boundaries between o-phase domains in order to provide evidence for the mixed-(R3m, $Pnm2_1$) phase inducement (Text S3 and Figure S14). When each $Pca2_1$ o-phase, $Pnm2_1$ o-phase, $P2_1/c$ m-phase, $P4_2/nmc$ t-phase, and R3m r-phase is positioned at the junction, the interface energy is calculated to be 7.859 J/m^2, 6.141 J/m^2, 6.146 J/m^2, 5.812J/m^2, and 5.910J/m^2, respectively. The result that the lowest interface energies are associated with the t-phase and r-phase supports the claim that the existence of a high symmetry phase at the grain boundary is the most stable. Then, the structural changes are compared after placing the t-phase and the r-phase between the o-phase domains, similar to the STEM data. Contrary to the case of the t-phase, where the deformation of the o-phase domain is severe, the structure is maintained stably in the case of the r-phase. These theoretical results indicate that r-phase is the most stable phase at the interface and the phase structurally stabilizes the o-phase.

Stabilization of the ferroelectric phase by interphase boundaries[32] and inducement of the polar phase at twinned monoclinic phase boundaries[36] have been studied in HfO_2 films/colloids. Our observation that the polar phase exists near boundaries between orthorhombic grains indicates that the atomic interaction at the grain boundaries plays an important role in understanding the ferroelectric properties in HfO_2 films.

We then considered the in-plane compressive strain observed in AR-STEM analysis in Figure 4d. As the width of the mixed-(R3m, $Pnm2_1$) phase between two domains decreases, a stronger

out-of-plane tensile strain in the <111> direction will be generated. The elongated {111} lattice drastically increases the amplitude of Γ_{15}^{x}, Γ_{15}^{y}, and Γ_{15}^{z} phonons, meaning the enhancement of ferroelectricity as shown in Figure 4e, in the same manner as in the previous study.[19] Although Wei et al. argued that a robust ferroelectric r-phase was evolved by in-plane compressive strain,[19] Zhang et al. pointed out that a relatively large strain (~5%) had to be applied to reach the experimentally observed polarization.[37] Our results suggest that the in-plane strain value exceeds 10% at the grain boundaries where the mixed-(R3m, $Pnm2_1$) phase is observed and that these boundary regions contribute a significant amount of polarization for the film.

To figure out the effect of these Hf defects on the interfacial ferroelectricity, we introduced the Hf vacancy (V_{Hf}) in our merged grain boundaries model as depicted in Figure S15a. In similar manner to our analysis in the main text, we calculated the phonon amplitudes of polar phonons (Γ_x, Γ_y, and Γ_z) and Γ along c direction (Γ_c) via phonon decomposition method. In the case without V_{Hf}, the amplitudes of polar phonons increase according to the increase of tensile strain along *c*-axis (Figure S15b), as we discussed in the main text. Notably, this increase in phonon amplitudes persisted even with V_{Hf} present (Figure S15c), showing similar tendency to the case without $V_{Hf.}$ The result indicates consistent behavior of polar phonon modes under tensile strain along *c*-axis.

Phase Transformation According to Thickness

Since the ferroelectric Y:HfO_2 film is composed of an in-plane network of nanoscale domains with distinct boundary structures and typically has a thickness of several to tens of nanometers, understanding the initiation and the growth of the domain structures is important. This is challenging to probe because of the small film thickness. In-plane high-resolution observation provides an opportunity to investigate how the crystallographic phase distribution changes as the film thickness varies. Free-standing Y:HfO_2 films synthesized with different thicknesses,

1.5 nm, 5.5 nm, and 11 nm, were analyzed using high-resolution (HR)-TEM (Figure 5a). Overall, the size of grains increases and the crystallinity of the film improves as the film thickness increases. 12-fold symmetric electron diffraction patterns corresponding to the <110>/<220> directions of the o-phase (11 nm, 5.5 nm) or the <112>/<200> directions of the t-phase (1.5 nm) confirm that the films are epitaxially grown in $<111>_{\text{o-phase}}$ or $<021>_{\text{t-phase}}$ directions where the domains are rotated by 90° to each other.[19]

In-depth HR-TEM analysis was conducted to distinguish o- and t-phases in films with different thicknesses. HR-TEM of the 5.5 nm thick film shows the o-phase grains with an induced mixed-(R3m, $Pnm2_1$) phase at the grain boundaries, which is similar in morphology to the 11 nm thick films (Figure 5c). Furthermore, strain maps from GPA and real-space phase analysis show strong compressive strain at the boundaries similar to the 11 nm thick films (Figures 4a, 4b), as seen in Figure 5d. Meanwhile, we observed symmetric atomic arrangements in the HR-TEM images of the 1.5 nm thick films that match to the simulated [201] t-phase TEM image (Figure 5e), indicating that the t-phase grains are dominantly formed in 1.5 nm thick films. It is worth noting that this observation is direct evidence for the stabilization of the t-phase that can occur in ultra-thin films, which has been previously reported.[13] Unlike the 11 nm and 5.5 nm thick films, the strain around grain boundaries is not observed in the 1.5 nm film, as seen in Figure 5f. Strain maps for another direction are shown in Figure S16. AR-STEM images of 5.5 nm and 1.5 nm thick film are presented in Figure S17. In addition, X-ray diffraction shows a marginal shift of (111) peak, confirming that the phase with intrinsic strain is maintained during the transfer process (Figure S18). The thickness of the films is confirmed by cross-sectional HAADF-STEM images as shown in Figure S19. Phase transition simulations (PTS) with DFT calculations regarding surface energy support that the transition from t-phase to o-phase can occur at 3-4 nm thickness below 300 K, as shown in Figure 5b, which is consistent with previous reports.[13,38] P-V and I-V curves from 5.5 nm and 1.5 nm thick films

confirm that 5.5 nm thick films are ferroelectric while 1.5 nm thick films do not show ferroelectric behavior due to the tetragonal phase (Figure S20). In summary, t-phase grains are mainly formed at the beginning of the film growth due to their low surface energy. As the film growth progresses, growing domains make tight contact, resulting in strained boundaries in accordance with the evolution of the o-phase. Our results imply that the overall ferroelectricity of the Y:HfO_2 thin film and its structural origin should be understood with a consideration of the crystallographic phase distribution that is dependent on film thickness.

Direct Observation of Ferroelectric Domains

Taking advantage of executing in-plane TEM analysis of support-free HfO_2 film in understanding the origin of the ferroelectricity of HfO_2 film, as we notice above, we attempt to assess atomic ferroelectric domains in Y:HfO_2 thin films. We prepare (100)-oriented epitaxial films which can directly expose distinct shifts in oxygen atom positions and employ oxygen displacement mapping. In-plane iDPC-STEM enables mapping the displacement of oxygen atoms, which allows the identification of ferroelectric domains at the unit cell level. In order to clearly visualize the direction of the ferroelectric domains, an in-plane sample of 5.5 nm-Y:HfO_2 film grown epitaxially in the [100] direction, which is perpendicular to the oxygen displacement vector, was prepared following the same procedures mentioned above. The HAADF-STEM image shows that the thin film has an orthorhombic atomic arrangement of hafnium atoms in the [100] direction (Figure S21). The corresponding iDPC-STEM image clearly reveals the oxygen atomic column positions (Figure 6a and Figure S21). As a result, the deviation of oxygen atoms from the center of the hafnium unit cell is measured and visualized on the in-plane image.

Based on theoretical calculations, it has been suggested that a unit cell level ferroelectric domain could be formed due to the flat phonon band of ferroelectric HfO_2.[24] As shown in the ferroelectric domain map in Figures 6a, 6b, a number of sub-angstrom domain walls of the non-

polar spacer layer are observed. Interestingly, non-polar regions are found to be formed at the 90˚ domain walls. In the iDPC-STEM images of polar phase and non-polar phase, the positions of hafnium and oxygen atoms coincide with the atomic model of polar o-phase (Space group: $Pca2_1$) and non-polar phase, respectively (Figure 6c). Although we used a model of the t-phase with the $P4_2/nmc$ space group in the figure, it is more accurate to consider this region as an inactive $Pca2_1$ o-phase, rather than the t-phase. This result indicates that, in addition to 180˚ domain walls previously reported, 90˚ domain walls are formed with a finite thickness in conjunction with nearby non-polar regions. The DFT calculation showed that the phonon coupling between domains attached vertically induces suppression of polarization, which could be observed as almost non-polar domains (details are discussed in Text S2 and Figure S22). Our finding suggests that the difference between theoretical predictions and experimental data for ferroelectricity of HfO_2 thin films can be explained by suppression of polarization at vertical domain walls.[24]

Building on these insights, we have analyzed seven iDPC-STEM images (Figure S23), which offer a clear view of oxygen displacement. Our findings suggest that approximately 73% of the ferroelectric domains were active. However, the domain activity significantly varied across different regions, possibly due to influences such as 90˚ domain walls. The average displacement of oxygen atoms at the active domains, as derived from the domain maps, was 0.646 Å. The calculated polarization from these figures amounts to 45 μC/cm². Yet, it is important to underline that making a direct connection between the domain maps from iDPC-STEM images and the net polarization of the entire film is not readily possible.

There are a few papers reporting ferroelectric domain walls in HfO_2 films based on theoretical calculations.[39,40] However, direct microscopic observation for tail-to-tail and head-to-head domain walls is limited due to technical difficulties in mapping oxygen displacement. The domain map displayed in Figure 6d reveals a random distribution of domain walls confined by

spacer layers. These layers act as protective barriers, preventing the propagation of charged domain walls and transforming them into charged domain points. A closer examination of these walls, as depicted in Figure 6e and Figure S24, indicates that their widths range from zero to eight unit-cells. The spacer layers not only inhibit domain interaction but also restrict the 180˚ charged domain walls, further emphasizing their role in the overall domain configuration. This finding highlights the importance of understanding the complex interplay between spacer layers and domain walls, as it is a part of important underlying mechanisms that govern the ferroelectric behavior of HfO_2 films, which can ultimately lead to improved performance in various applications.

Conclusion

We have investigated the interactions of grains and ferroelectric domains in epitaxially grown free-standing ferroelectric Y:HfO_2 films. By 4D-STEM and AR-STEM, we find that HS-phase with in-plane compressive strain is induced at the boundaries between (111)-oriented ferroelectric grains. DFT calculations demonstrate that this boundary phase enhances polarization with out-of-plane tensile strain. Additionally, it is found that 1.5 nm thick film is mainly composed of the t-phase, while 5.5 nm and 11 nm thick films consist of ferroelectric domain networks. It is also revealed that polarization is suppressed at the vertical domain wall and charged domain walls are confined by spacer layers. For device engineering, strategies to minimize 90° domain walls include tailoring growth conditions and substrate orientation. The HS-phase properties at grain boundaries could enable improved device designs. Our results provide insights into understanding the complex domain network of HfO_2-based ferroelectric films. These findings also enlighten that device engineering based on ferroelectric HfO_2 film needs fine controls of the growth condition, such as types and orientations of the substrate, the use of buffer layer, temperature, and confinement, and post-synthesis treatment, in a level to

manage nanoscale domain networks. Such high-precision fabrication of the ferroelectric HfO_2 film could be achieved with a combination of the large-area in-plane structure analysis, as introduce here, and theoretical calculation including interaction with electrodes, impact of strain, effect of doping, and more. In addition, it is worth mentioning that the overall analysis platform we introduce here has a potential to answer important questions that remains in the HfO_2 based ferroelectrics. Future studies may focus on effect of polling or wake-up on domain network structures. These can be investigated by imaging in-plane TEM samples using Piezoresponse Force Microscopy (PFM), or by employing in-situ biasing during in-plane TEM imaging. By this way, it will provide insights into the behavior of domains under different electrical conditions.

METHODS

Sample fabrication and electrical measurements

7% Y-doped HfO_2 thin films were grown by pulsed laser deposition (PLD) on a 0.5wt% Nb-doped STO (001) substrate. Before the growth of Y:HfO_2 films, the LSMO buffer electrodes were grown on the substrate. A KrF excimer laser with a wavelength of 248 nm, an energy density of 2 J/cm^2, and a frequency of 6 Hz was used. The (111)-oriented Y:HfO_2 film and LSMO film were deposited at 700 ℃ under oxygen at a partial pressure of 150 mTorr. The (100)-oriented Y:HfO_2 film was deposited under oxygen at a partial pressure of 1 mTorr. the electrical measurements, square-shaped 45×45 μm Pt (30 nm) top electrodes were deposited by using an e-beam evaporator. Polarization hysteresis curves as a function of voltage were conducted using a semiconductor parameter analyzer (4200-SCS; Keithley Instruments, Cleveland, OH, USA).

Release and transfer of films

For fabrication of the free-standing films, poly(methyl methacrylate) (PMMA) chlorobenzene solution was spin-coated and polypropylene carbonate (PCC) anisole solution was drop-casted on the films and dried as polymer support. Subsequently, the films were immersed into the KI + HCl aqueous solution to dissolve the LSMO layer. The floated free-standing films were washed twice with DI water and were scooped with holey carbon grids or other substrates. The films were dried under 40 ℃ for an hour to remove water and adhere to the grids/substrates. The polymer layer was dissolved by sinking in acetone for a day.

(S)TEM, 4D-STEM, automated STEM and iDPC-STEM measurements

For HR-TEM and AR-STEM analysis, the Y:HfO_2 films on holey carbon grids were investigated using an aberration-corrected JEM-ARM200F (Cold FEG, JEOL Ltd, Japan) microscope equipped with a high-angle annular dark-field scanning transmission electron microscope (HAADF-STEM) and a JEOL-2100F (Cold FEG, JEOL Ltd, Japan) microscope operating at 200 kV. The 4D-STEM and automated AR-STEM were accomplished using a Thermo Fischer aberration corrected Titan 80-300 operated at 300 kV for Y:HfO_2 films on holey silicon nitride grids. 4D-STEM experiments used a 1 mrad convergence angle and ~1 nA of beam current. A direct electron detector with 87,000 Hz frame rate and 576×576 pixels was used to record 1024×1024 probe positions resulting in a 700 GB data set. Each frame was processed using the National Energy Research Scientific Computing Center (NERSC) high performance computer to find single electron events (called electron counting) using algorithms available in the stempy software package. The resulting sparse data was analyzed by custom python algorithms to create virtual dark field images presented in the paper.

The automated AR-STEM images were acquired using a 30 mrad convergence angle and ~35 pA of beam current. The microscope hosts a custom built all-piezo driven sample stage with custom written automation software capable of centering, imaging, and focusing at high

resolution. A grid of 7×7 stage positions was programmed and a 2048×2048 pixel image acquired at every stage position. Position accuracy for each stage position was set to 6 nm to speed up the data acquisition, which is why some images are not at the desired perfect grid positions. The set of images span a range of ~220 nm with a field of view of 31.3 nm per image (0.0153 nm/pixel) and the full experiment took approximately 2 hours.

For iDPC-STEM, the Y:HfO_2 films on holey silicon nitride grids were investigated using an aberration-corrected monochromated Themis Z (X-FEG, Thermo Fisher, USA) microscope operating at 300 kV. All TEM grids with the transferred materials were cleaned by ion cleaning and electron beam showering to eliminate the residual contaminants.

Strain mapping was carried out using Gatan DigitalMicrograph software. Geometric Phase Analysis was conducted using GPA v4.10 plugin in DigitalMicrograph.[41] Analyses were performed on {110} reflections using a cosine mask type.

STEM and TEM Simulations

STEM simulation was carried out by Prismatic software.[42,43] TEM simulation was performed with Kirkland with COMPUTEM software.[44] First, we used Vesta software to construct HfO_2 unit cell orienting [111]. Then the STEM and TEM simulated parameters were set with the accelerating voltage of 300 kV, pixel size of 0.05 Å, potential bound of 2 Å, probe semi-angle of 17 mrad, detector range of 10-40 mrad for ABF and 60-90 mrad for HAADF. We also set the number of frozen phonons to 32, and a probe step to 0.2 Å to precisely generate the images. Noise was added with ImageJ software for realistic images.

Atomic resolution displacement and strain analysis

The AR-STEM images were used for atomic resolution strain analysis. First, a peak finding algorithm was used to find the position of every Hf atom within a field of view near the grain boundary as defined in the *peak_find.peakFind2D* function of the *ncempy* Python package.

Every peak was then fit to a two-dimensional Gaussian function to improve the accuracy of its location. Lattice vectors were then fit to the atom positions to generate a U and V lattice corresponding to the average unit cell spacings and angles. These lattice vectors were used to determine the ideal position of each unit cell in the image. HfO_2 does not have a simple structure, and thus it was required to generate extra atoms at positions within each unit cell to match the structure expected along the <111> zone axis. The ideal lattice could then be compared with experimental atom positions. The difference between the expected and ideal lattice sites were calculated and strain along the U and V directions was calculated using nearest neighbors to estimate the local differential of the displacement. The strain values for each atomic site were interpolated onto a cartesian grid using the *ndimage.map_coordinates* function in the Python package *scipy*. The strain maps were blurred with a Gaussian function to remove noise.

ASSOCIATED CONTENT

Supporting Information.

This material is available free of charge via the Internet at http://pubs.acs.org.

Experimental details, description of DFT simulation data and supporting figures (PDF).

AUTHOR INFORMATION

Author Contributions

K.P., K.L., S.C.C., and J.P. planned the experimental portion of the research. H.J.L., C.K., and J.H.L. planned the theoretical portion of the research. K.P., D.K., J.K., S.K., A.L., A.P., H.C., P.E., and J.P. conducted the TEM analysis of experimental data. A.L., A.P., and P.E. conducted

4D-STEM and analysis of experimental data. A.L., A.P., W.T., and P.E. conducted automated STEM and analysis of experimental data. K.L. and S.C.C. conducted the deposition of the films and electrical analysis of experimental data. K.P., D.K., and J.P. developed the analysis methods of the experimental data. K.P., D.K., K.L., H.J.L., P.E., J.H.L., S.C.C., and J.P. wrote the manuscript. S.C.C. and J.P. supervised the experimental research. J.H.L. supervised the theoretical research. All authors contributed to the discussion of results.

Notes

The authors declare no competing financial interest.

ACKNOWLEDGMENT

We would like to thank Gatan, Inc. as well as P. Denes, A. Minor, J. Ciston, C. Ophus, J. Joseph, and I. Johnson who contributed to the development of the 4D Camera. **Funding:** This work was supported by the Institutes for Basic Science (IBS-R006-D1) (J.P.), the National Research Foundation of Korea (NRF) grant funded by the Korean government (Ministry of Science and ICT) (No. RS-2023-00283902) (J.P.). EM analysis, material characterization, and EM simulation are supported by Samsung Research Funding & Incubation Center of Samsung Electronics under Project Number SRFC-MA2002-03 (J.P.). S.C. was supported partly by the National Research Foundation of Korea grant funded by the Korean government Ministry of Science and ICT (MSIT) (Grants Nos. NRF-2020M3F3A2A01081594 and NRF-2021R1A2C1094795). Part of this study was performed using the facilities of the Institute for Basic Science (IBS) Center for Correlated Electron Systems, Seoul National University. J.H.L. acknowledges the support of the National Research Foundation of Korea grant funded by the Korean Government Ministry of Science and ICT (MSIT) (Grants Nos. NRF-2022M3F3A2A01079710, NRF-2020R1A2C2103126, NRF-RS-2024-00404361, NRF-RS-

2023-00257666, and NRF-RS-2023- 00218799). The experiments were performed at the Molecular Foundry, Lawrence Berkeley National Laboratory, which is supported by the U.S. Department of Energy under contract no. DE-AC02-05CH11231. This work was partially funded by the U.S. Department of Energy in the program "4D Camera Distillery: From Massive Electron Microscopy Scattering Data to Useful Information with AI/ML."

References

(1) Böscke, T. S.; Müller, J.; Bräuhaus, D.; Schröder, U.; Böttger, U. Ferroelectricity in Hafnium Oxide Thin Films. *Applied Physics Letters* **2011**, 99, 102903.

(2) Cheema, S. S.; Shanker, N.; Wang, L.-C.; Hsu, C.-H.; Hsu, S.-L.; Liao, Y.-H.; Jose, M. S.; Gomez, J.; Chakraborty, W.; Li, W.; Bae, J.-H.; Volkman, S. K.; Kwon, D.; Rho, Y.; Pinelli, G.; Rastogi, R.; Pipitone, D.; Stull, C.; Cook, M.; Tyrrell, B.; Stoica, V. A.; Zhang, Z.; Freeland, J. W.; Tassone, C. J.; Mehta, A.; Saheli, G.; Thompson, D.; Suh, D. I.; Koo, W.-T.; Nam, K.-J.; Jung, D. J.; Song, W.-B.; Lin, C.-H.; Nam, S.; Heo, J.; Parihar, N.; Grigoropoulos, C. P.; Shafer, P.; Fay, P.; Ramesh, R.; Mahapatra, S.; Ciston, J.; Datta, S.; Mohamed, M.; Hu, C.; Salahuddin, S. Ultrathin Ferroic HfO_2–ZrO_2 Superlattice Gate Stack for Advanced Transistors. *Nature* **2022**, 604 (7904), 65–71.

(3) Kang, S.; Jang, W.-S.; Morozovska, A. N.; Kwon, O.; Jin, Y.; Kim, Y.-H.; Bae, H.; Wang, C.; Yang, S.-H.; Belianinov, A.; Randolph, S.; Eliseev, E. A.; Collins, L.; Park, Y.; Jo, S.; Jung, M.-H.; Go, K.-J.; Cho, H. W.; Choi, S.-Y.; Jang, J. H.; Kim, S.; Jeong, H. Y.; Lee, J.; Ovchinnikova, O. S.; Heo, J.; Kalinin, S. V.; Kim, Y.-M.; Kim, Y. Highly Enhanced Ferroelectricity in HfO_2-Based Ferroelectric Thin Film by Light Ion Bombardment. *Science* **2022**, 376 (6594), 731–738.

(4) Cheema, S. S.; Shanker, N.; Hsu, S.-L.; Rho, Y.; Hsu, C.-H.; Stoica, V. A.; Zhang, Z.; Freeland, J. W.; Shafer, P.; Grigoropoulos, C. P.; Ciston, J.; Salahuddin, S. Emergent Ferroelectricity in Subnanometer Binary Oxide Films on Silicon. *Science* **2022**, 376 (6593), 648–652.

(5) Jeong, D. S.; Hwang, C. S. Nonvolatile Memory Materials for Neuromorphic Intelligent Machines. *Advanced Materials* **2018**, 30, 1704729.

(6) Han, W.; Zheng, X.; Yang, K.; Tsang, C. S.; Zheng, F.; Wong, L. W.; Lai, K. H.; Yang, T.; Wei, Q.; Li, M.; Io, W. F.; Guo, F.; Cai, Y.; Wang, N.; Hao, J.; Lau, S. P.; Lee, C.-S.; Ly, T. H.; Yang, M.; Zhao, J. Phase-Controllable Large-Area Two-Dimensional In_2Se_3 and Ferroelectric Heterophase Junction. *Nature Nanotechnology* **2022**, 18 (1), 55–63.

(7) Song, M.-K.; Kang, J.-H.; Zhang, X.; Ji, W.; Ascoli, A.; Messaris, I.; Demirkol, A. S.; Dong, B.; Aggarwal, S.; Wan, W.; Hong, S.-M.; Cardwell, S. G.; Boybat, I.; Seo, J.-S.; Lee, J.-S.; Lanza, M.; Yeon, H.; Onen, M.; Li, J.; Yildiz, B.; Del Alamo, J. A.; Kim, S.; Choi, S.; Milano, G.; Ricciardi, C.; Alff, L.; Chai, Y.; Wang, Z.; Bhaskaran, H.; Hersam, M. C.; Strukov, D.; Wong, H. -s. P.; Valov, I.; Gao, B.; Wu, H.; Tetzlaff, R.; Sebastian, A.; Lu, W.; Chua, L.; Yang, J. J.; Kim, J. Recent Advances and Future Prospects for Memristive Materials, Devices, and Systems. *ACS Nano* **2023**, 17 (13), 11994–12039.

(8) Yang, S. Y.; Seidel, J.; Byrnes, S. J.; Shafer, P.; Yang, C. -h.; Rossell, M. D.; Yu, P.; Chu, Y. -h.; Scott, J. F.; Ager, J. W.; Martin, L. W.; Ramesh, R. Above-Bandgap Voltages from Ferroelectric Photovoltaic Devices. *Nature Nanotechnology* **2010**, 5 (2), 143–147.

(9) Park, M. H.; Lee, Y. H.; Kim, H. J.; Kim, Y. J.; Moon, T.; Kim, K. D.; Müller, J.; Kersch, A.; Schroeder, U.; Mikolajick, T.; Hwang, C. S. Ferroelectricity and Antiferroelectricity of Doped Thin HfO_2-Based Films. *Advanced Materials* **2015**, 27 (11), 1811–1831.

(10) Khan, A. I.; Chatterjee, K.; Wang, B.; Drapcho, S.; You, L.; Serrao, C.; Bakaul, S. R.; Ramesh, R.; Salahuddin, S. Negative Capacitance in a Ferroelectric Capacitor. *Nature Materials* **2014**, 14 (2), 182–186.

(11) Sang, X.; Grimley, E. D.; Schenk, T.; Schroeder, U.; LeBeau, J. M. On the Structural Origins of Ferroelectricity in HfO_2 Thin Films. *Applied Physics Letters* **2015**, 106 (16), 162905.

(12) Ohtaka, O.; Fukui, H.; Kunisada, T.; Fujisawa, T.; Funakoshi, K.; Utsumi, W.; Irifune, T.; Kuroda, K.; Kikegawa, T. Phase Relations and Volume Changes of Hafnia under High Pressure and High Temperature. *Journal of the American Ceramic Society* **2001**, 84 (6), 1369–1373.

(13) Park, M. H.; Lee, Y. H.; Kim, H. J.; Schenk, T.; Lee, W.; Kim, K. D.; Fengler, F. P. G.; Mikolajick, T.; Schroeder, U.; Hwang, C. S. Surface and Grain Boundary Energy as the Key Enabler of Ferroelectricity in Nanoscale Hafnia-Zirconia: A Comparison of Model and Experiment. *Nanoscale* **2017**, 9 (28), 9973–9986.

(14) Park, M. H.; Schenk, T.; Fancher, C. M.; Grimley, E. D.; Zhou, C.; Richter, C.; LeBeau, J. M.; Jones, J. L.; Mikolajick, T.; Schroeder, U. A Comprehensive Study on the Structural Evolution of HfO_2 Thin Films Doped with Various Dopants. *Journal of Materials Chemistry. C* **2017**, 5 (19), 4677–4690.

(15) Xu, X.; Huang, F. T.; Qi, Y.; Singh, S.; Rabe, K. M.; Obeysekera, D.; Yang, J.; Chu, M. W.; Cheong, S. W. Kinetically Stabilized Ferroelectricity in Bulk Single-Crystalline HfO_2:Y. *Nature Materials* **2021**, 20 (6), 826–832.

(16) Fan, S.; Singh, S.; Xu, X.; Park, K.; Qi, Y.; Cheong, S. W.; Vanderbilt, D.; Rabe, K. M.; Musfeldt, J. L. Vibrational Fingerprints of Ferroelectric HfO_2. *Npj Quantum Materials* **2022**, 7, 32.

(17) Park, M. H.; Chung, C.; Schenk, T.; Richter, C.; Opsomer, K.; Detavernier, C.; Adelmann, C.; Jones, J. L.; Mikolajick, T.; Schroeder, U. Effect of Annealing Ferroelectric HfO_2 Thin Films: In Situ, High Temperature X-Ray Diffraction. *Advanced Electronic Materials* **2018**, 4 (7), 1800091.

(18) Grimley, E. D.; Schenk, T.; Sang, X.; Pešić, M.; Schroeder, U.; Mikolajick, T.; LeBeau, J. M. Structural Changes Underlying Field-Cycling Phenomena in Ferroelectric HfO_2 Thin Films. *Advanced Electronic Materials* **2016**, 2 (9), 1600173.

(19) Wei, Y.; Nukala, P.; Salverda, M.; Matzen, S.; Zhao, H.J.; Everhardt, A.; Blake, G.R.; Lecoeur, P.; Kooi, B.J.; Íñiguez, J.; Dkhil, B.; Noheda, B. A Rhombohedral Ferroelectric Phase in Epitaxially-Strained $Hf_{0.5}Zr_{0.5}O_2$ Thin Films. *Nature Materials* **2018**, 17 (12), 1095-1100.

(20) Wang, Y.; Tao, L.; Guzman, R.; Luo, Q.; Zhou, W.; Yang, Y.; Wei, Y.; Liu, Y.; Jiang, P.; Chen, Y.; Lv, S.; Ding, Y.; Wei, W.; Gong, T.; Wang, Y.; Liu, Q.; Du, S.; Liu, M. A Stable Rhombohedral Phase in Ferroelectric $Hf(Zr)_{1+x}O_2$ Capacitor with Ultralow Coercive Field. *Science* **2023**, 381 (6657), 558–563.

(21) Park, M. H.; Kim, H. J.; Kim, Y. J.; Lee, Y. H.; Moon, T.; Kim, K. D.; Hyun, S. D.; Hwang, C. S. Study on the Size Effect in $Hf_{0.5}Zr_{0.5}O_2$ Films Thinner than 8 nm before and after Wake-Up Field Cycling. *Applied Physics Letters* **2015**, 107 (19), 192907.

(22) Cheema, S. S.; Kwon, D.; Shanker, N.; Reis, R. D.; Hsu, S. L.; Xiao, J.; Zhang, H.; Wagner, R.; Datar, A.; McCarter, M. R.; Serrao, C. R.; Yadav, A. K.; Karbasian, G.;

610 Hsu, C. H.; Tan, A. J.; Wang, L. C.; Thakare, V.; Zhang, X.; Mehta, A.; Karapetrova,
611 E.; Chopdekar, R. V.; Shafer, P.; Arenholz, E.; Hu, C.; Proksch, R.; Ramesh, R.;
612 Ciston, J.; Salahuddin, S. Enhanced Ferroelectricity in Ultrathin Films Grown Directly
613 on Silicon. *Nature* **2020**, 580 (7804), 478–482.

614 (23) Zhou, Y.; Wu, D.; Zhu, Y.; Cho, Y.; He, Q.; Yang, X.; Herrera, K.; Chu, Z.; Han, Y.;
615 Downer, M. C.; Peng, H.; Lai, K. Out-of-Plane Piezoelectricity and Ferroelectricity in
616 Layered α-In_2Se_3 Nanoflakes. *Nano Letters* **2017**, 17 (9), 5508–5513.

617 (24) Lee, H.-J.; Lee, M.; Lee, K.; Jo, J.; Yang, H.; Kim, Y.; Chae, S. C.; Waghmare, U.;
618 Lee, J. H. Scale-Free Ferroelectricity Induced by Flat Phonon Bands in HfO_2. *Science*
619 **2020**, 369 (6509), 1343–1347.

620 (25) Bakaul, S. R.; Serrao, C. R.; Lee, M.; Yeung, C. W.; Sarker, A.; Hsu, S. L.; Yadav, A.
621 K.; Dedon, L.; You, L.; Khan, A. I.; Clarkson, J. D.; Hu, C.-M.; Ramesh, R.;
622 Salahuddin, S. Single Crystal Functional Oxides on Silicon. *Nature Communications*
623 **2016**, 7 (1), 10547.

624 (26) Zhong, H.; Li, M.; Zhang, Q.; Yang, L.; He, R.; Liu, F.; Liu, Z.; Li, G.; Sun, Q.; Xie,
625 D.; Meng, F.; Li, Q.; He, M.; Guo, E.; Wang, C.; Zhong, Z.; Wang, X.; Gu, L.; Yang,
626 G.; Jin, K.; Gao, P.; Ge, C. Large-Scale $Hf_{0.5}Zr_{0.5}O_2$ Membranes with Robust
627 Ferroelectricity. *Advanced Materials* **2022**, 34 (24), 2109889.

628 (27) Fan, S.-T.; Chen, Y.-W.; Liu, C. W. Strain Effect on the Stability in Ferroelectric HfO_2
629 Simulated by First-Principles Calculations. *Journal of Physics. D, Applied Physics*
630 **2020**, 53 (23), 23LT01.

(28) Ophus, C. Four-Dimensional Scanning Transmission Electron Microscopy (4D-STEM): From Scanning Nanodiffraction to Ptychography and Beyond. *Microscopy and Microanalysis* **2019**, 25 (3), 563–582.

(29) Jiang, Y.; Chen, Z.; Han, Y.; Deb, P.; Gao, H.; Xie, S.; Purohit, P.; Tate, M. W.; Park, J.; Gruner, S. M.; Elser, V.; Muller, D. A. Electron Ptychography of 2D Materials to Deep Sub-ångström Resolution. *Nature* **2018**, 559 (7714), 343–349.

(30) Spurgeon, S. R.; Ophus, C.; Jones, L.; Petford-Long, A.; Kalinin, S. V.; Olszta, M. J.; Dunin-Borkowski, R. E.; Salmon, N.; Hattar, K.; Yang, W. C. D.; Sharma, R.; Du, Y.; Chiaramonti, A.; Zheng, H.; Buck, E. C.; Kovarik, L.; Penn, R. L.; Li, D.; Zhang, X.; Murayama, M.; Taheri, M. L. Towards Data-Driven Next-Generation Transmission Electron Microscopy. *Nature Materials* **2020**, 20 (3), 274–279.

(31) Kalinin, S. V.; Ziatdinov, M.; Hinkle, J.; Jesse, S.; Ghosh, A.; Kelley, K. P.; Lupini, A. R.; Sumpter, B. G.; Vasudevan, R. K. Automated and Autonomous Experiments in Electron and Scanning Probe Microscopy. *ACS Nano* **2021**, 15 (8), 12604–12627.

(32) Yun, Y.; Buragohain, P.; Li, M.; Ahmadi, Z.; Zhang, Y.; Li, X.; Wang, H.; Li, J.; Lu, P.; Tao, L.; Wang, H.; Shield, J. E.; Tsymbal, E. Y.; Gruverman, A.; Xu, X. Intrinsic Ferroelectricity in Y-Doped HfO_2 Thin Films. *Nature Materials* **2022**, 21 (8), 903–909.

(33) Chason, E.; Guduru, P. R. Tutorial: Understanding Residual Stress in Polycrystalline Thin Films through Real-Time Measurements and Physical Models. *Journal of Applied Physics* **2016**, 119 (19), 191101.

(34) Abadias, G.; Chason, E.; Keckes, J.; Sebastiani, M.; Thompson, G. B.; Barthel, E.; Doll, G. L.; Murray, C. E.; Stoessel, C. H.; Martinu, L. Review Article: Stress in Thin

Films and Coatings: Current Status, Challenges, and Prospects. *Journal of Vacuum Science & Technology. A. Vacuum, Surfaces, and Films* **2018**, 36 (2), 020801.

(35) Yu, H. Z.; Thompson, C. V. Grain Growth and Complex Stress Evolution during Volmer–Weber Growth of Polycrystalline Thin Films. *Acta Materialia* **2014**, 67, 189–198.

(36) Du, H.; Groh, C.; Jia, C.-L.; Ohlerth, T.; Dunin-Borkowski, R. E.; Simon, U.; Mayer, J. Multiple Polarization Orders in Individual Twinned Colloidal Nanocrystals of Centrosymmetric HfO_2. *Matter* **2021**, 4 (3), 986–1000.

(37) Zhang, Y.; Yang, Q.; Tao, L.; Tsymbal, E. Y.; Alexandrov, V. Effects of Strain and Film Thickness on the Stability of the Rhombohedral Phase of HfO_2. *Physical Review Applied* **2020**, 14 (1), 014068.

(38) Park, M. H.; Lee, Y. H.; Kim, H. J.; Kim, Y. J.; Moon, T.; Kim, K. D.; Hyun, S. D.; Mikolajick, T.; Schroeder, U.; Hwang, C. S. Understanding the Formation of the Metastable Ferroelectric Phase in Hafnia–Zirconia Solid Solution Thin Films. *Nanoscale* **2018**, 10 (2), 716–725.

(39) Ding, W.; Zhang, Y.; Tao, L.; Yang, Q.; Zhou, Y. The Atomic-Scale Domain Wall Structure and Motion in HfO_2-Based Ferroelectrics: A First-Principle Study. *Acta Materialia* **2020**, 196, 556–564.

(40) Zhou, P.; Zeng, B.; Yang, W.; Liao, J.; Meng, F.; Zhang, Q.; Gu, L.; Zheng, S.; Liao, M.; Zhou, Y. Intrinsic 90° Charged Domain Wall and Its Effects on Ferroelectric Properties. *Acta Materialia* **2022**, 232, 117920.

(41) Hÿtch, M. J.; Putaux, J.-L.; Pénisson, J.-M. Measurement of the Displacement Field of Dislocations to 0.03 Å by Electron Microscopy. *Nature* **2003**, 423 (6937), 270–273.

(42) Pryor, A.; Ophus, C.; Miao, J. A Streaming Multi-GPU Implementation of Image Simulation Algorithms for Scanning Transmission Electron Microscopy. *Advanced Structural and Chemical Imaging* **2017**, 3 (1), 15.

(43) Li, Z.; Rose, H.; Madsen, J.; Biskupek, J.; Susi, T.; Kaiser, U. Computationally Efficient Handling of Partially Coherent Electron Sources in (S)TEM Image Simulations via Matrix Diagonalization. *Microscopy and Microanalysis* **2023**, 29 (1), 364–373.

(44) Kirkland, E. J. *Advanced computing in Electron Microscopy*, 2nd Edition; Springer: New York, **2010**; pp. 1-269.

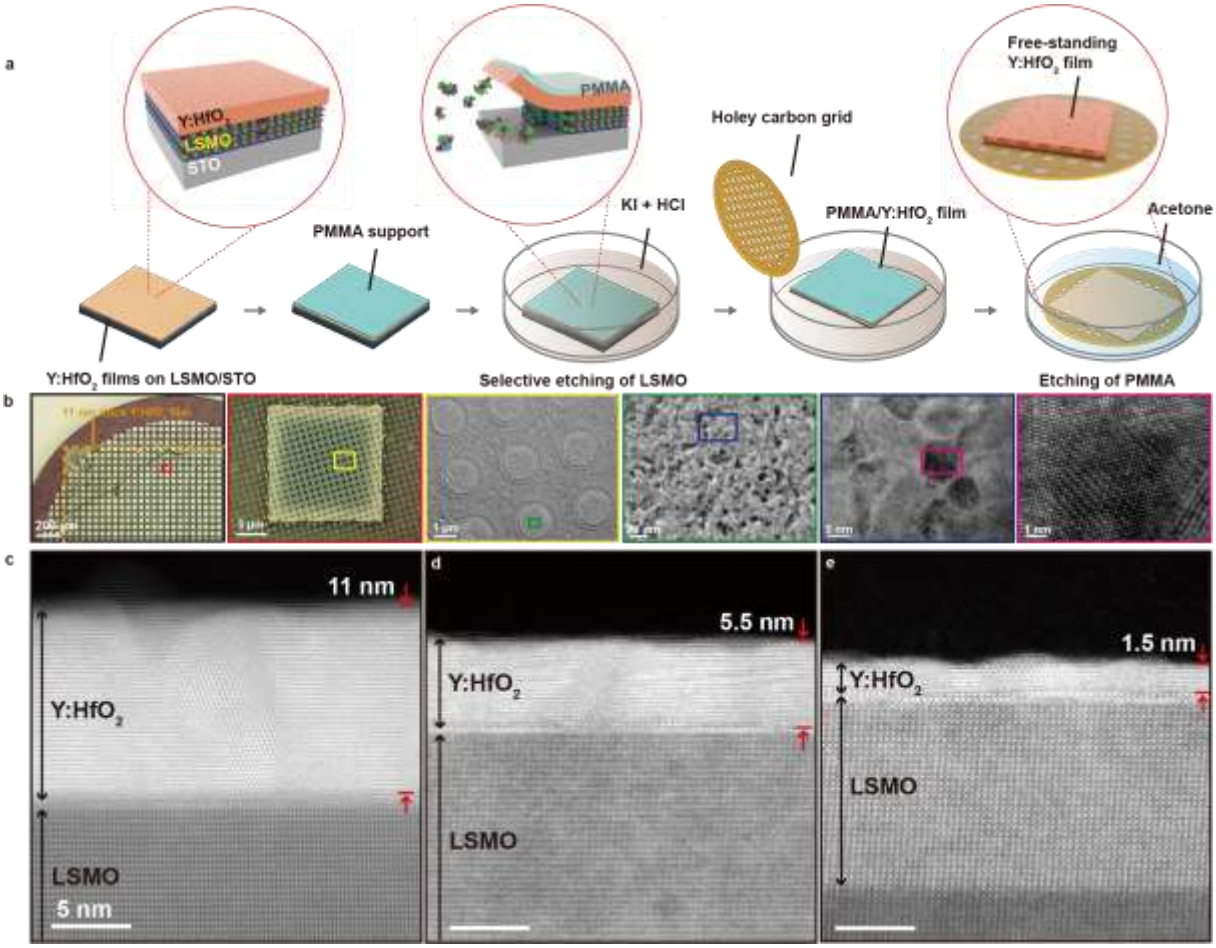

Figure 1. Free-standing ferroelectric Y:HfO_2 thin films for in-plane analysis. (a) A scheme for the preparation of a free-standing ferroelectric Y:HfO_2 film on a holey carbon grid. (b) Optical microscopy and TEM images of an 11 nm Y:HfO_2 film transferred onto a TEM grid; the rectangle in each image is the viewing area for the next image. (c-e) The cross-sectional STEM images of (c) 11 nm, (d) 5.5 nm, (e) 1.5 nm thick films, which are intensively analyzed, showing overlapping information of grains.

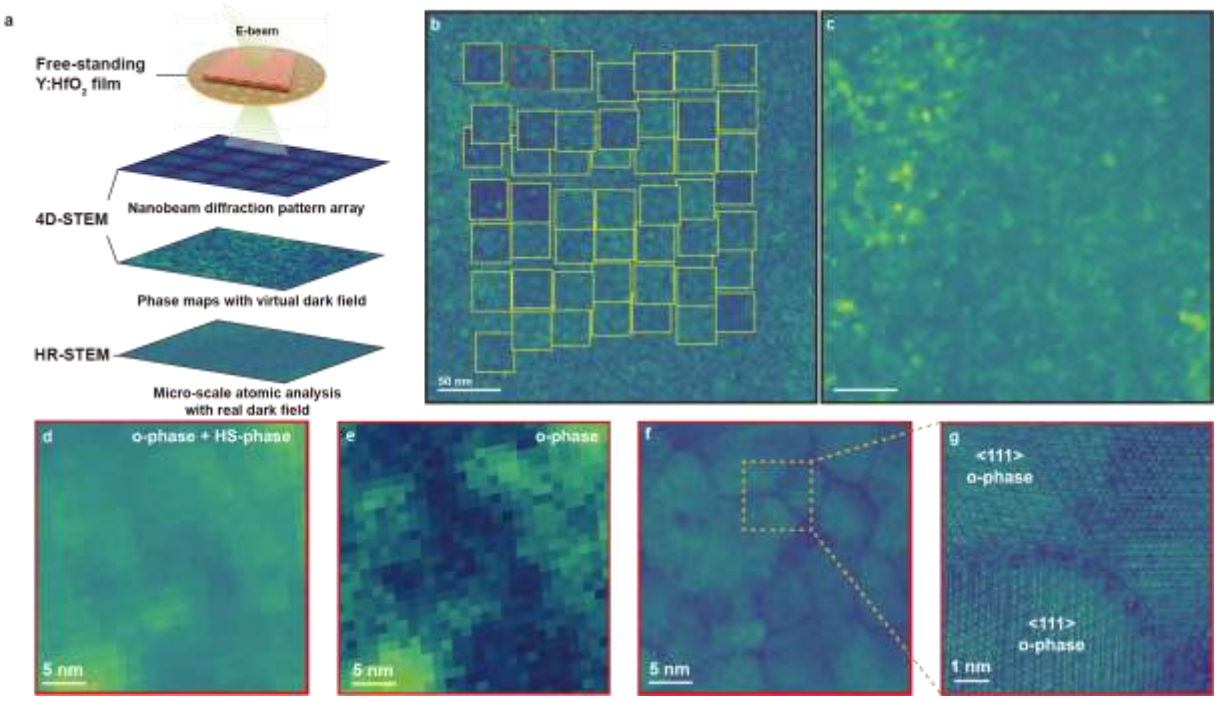

Figure 2. In-plane electron microscopic analysis on ferroelectric Y:HfO_2 thin films. (a) A scheme for 4D-STEM and AR-STEM analysis on a free-standing ferroelectric Y:HfO_2 film. (b) Micrometer-scale AR-STEM image using automated STEM; each rectangle represents an imaging area. (c) 4D-STEM integrated intensity map corresponding to (b). (d and e) Virtual dark field (VDF) images showing phase distributions from a red rectangle in (b). (f and g) Corresponding HAADF-STEM image and a magnified image.

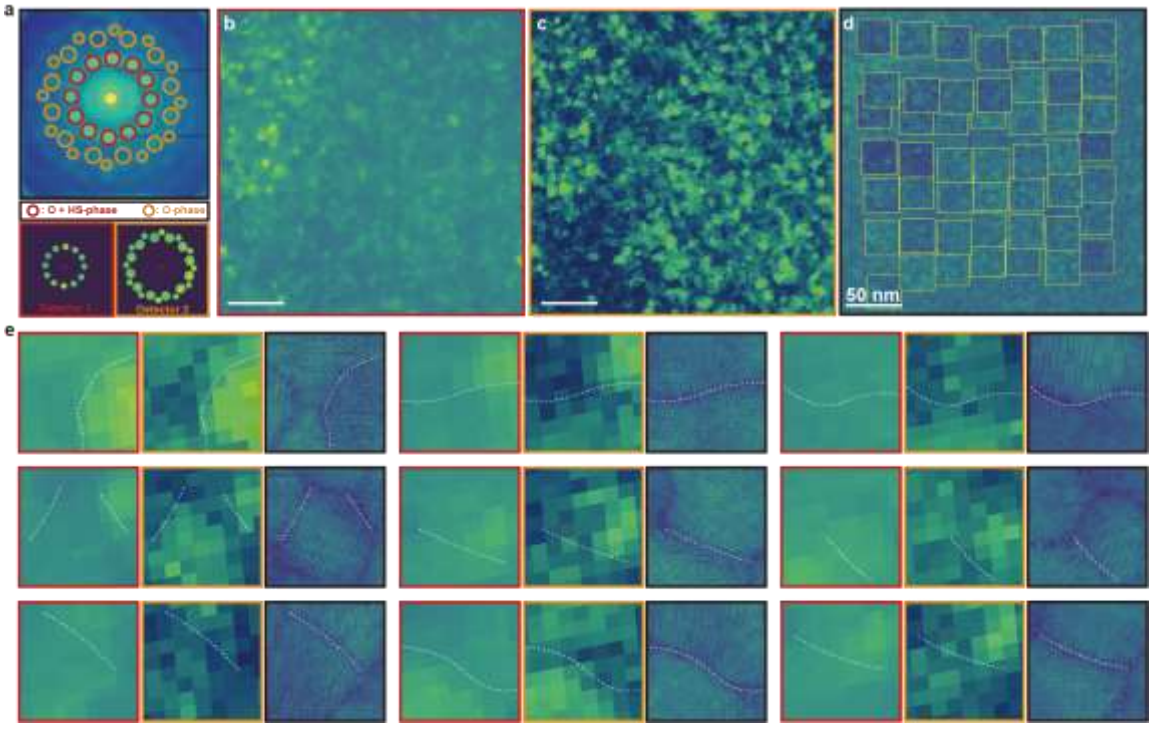

Figure 3. 4D-STEM and AR-STEM observation of domain distribution and strained polar mixed-(R3m, $Pnm2_1$) phase at grain boundaries. (a) The mean diffraction pattern of the 11 nm Y:HfO_2 film acquired by nanobeam 4D-STEM; discs from both o-phase and HS-phase are indicated with red circles while peaks from only o-phase are indicated with orange circles. The arrangement of the red and orange circles determines the shape of virtual detectors 1 and 2, respectively. (b-d) Corresponding (b) VDF images with detector 1, (c) VDF images with detector 2 and (d) large-area automated AR-STEM images. (e) 9 sets of 4D-STEM and AR-STEM images of the grain boundaries where the signal from detector 2 is low and the signal from detector 1 is high. Each set consists of three images: VDF1 (left), VDF2 (center), and AR-STEM (right).

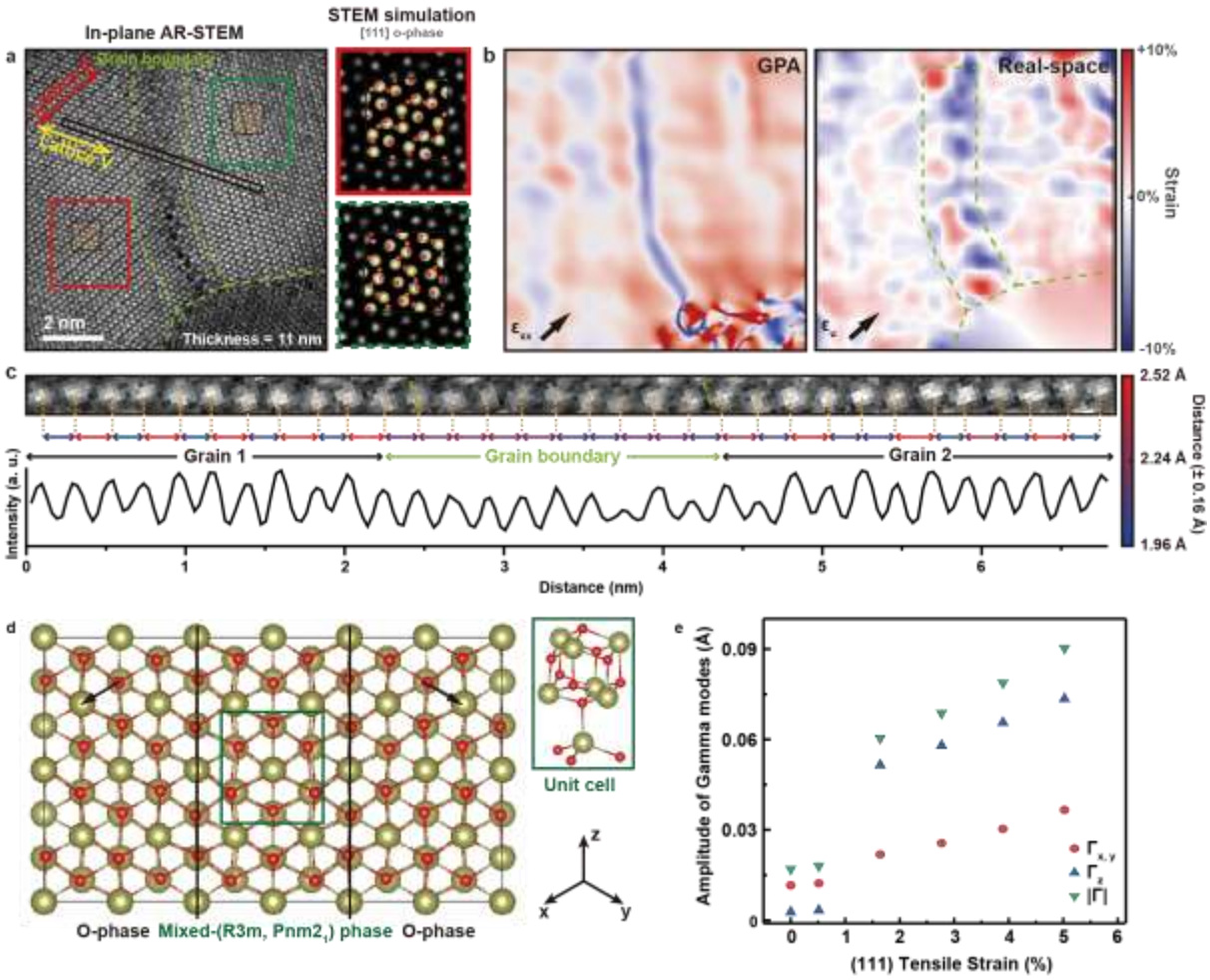

715

716 **Figure 4.** Experimental observation and theoretical calculations of strained polar mixed-(R3m,
717 $Pnm2_1$) phase at grain boundaries. (a) AR-STEM images with the o-phase atomic model and
718 simulation of [111] zone axis. Directions of lattice u and v are shown in red and yellow arrows,
719 respectively. (b) Corresponding strain maps from GPA and the real-space phase analysis. (c)
720 The intensity profile of the black box in (a). (d) Atomic arrangement based on DFT calculations.
721 Black arrows in o-phase regions indicate [001] and the green area is the unit cell of the relaxed
722 structure. (e) Change in the amplitude of $\Gamma_{15}^{x}, \Gamma_{15}^{y}$, and Γ_{15}^{z} phonon modes according to tensile
723 strain in {111} lattices.

724

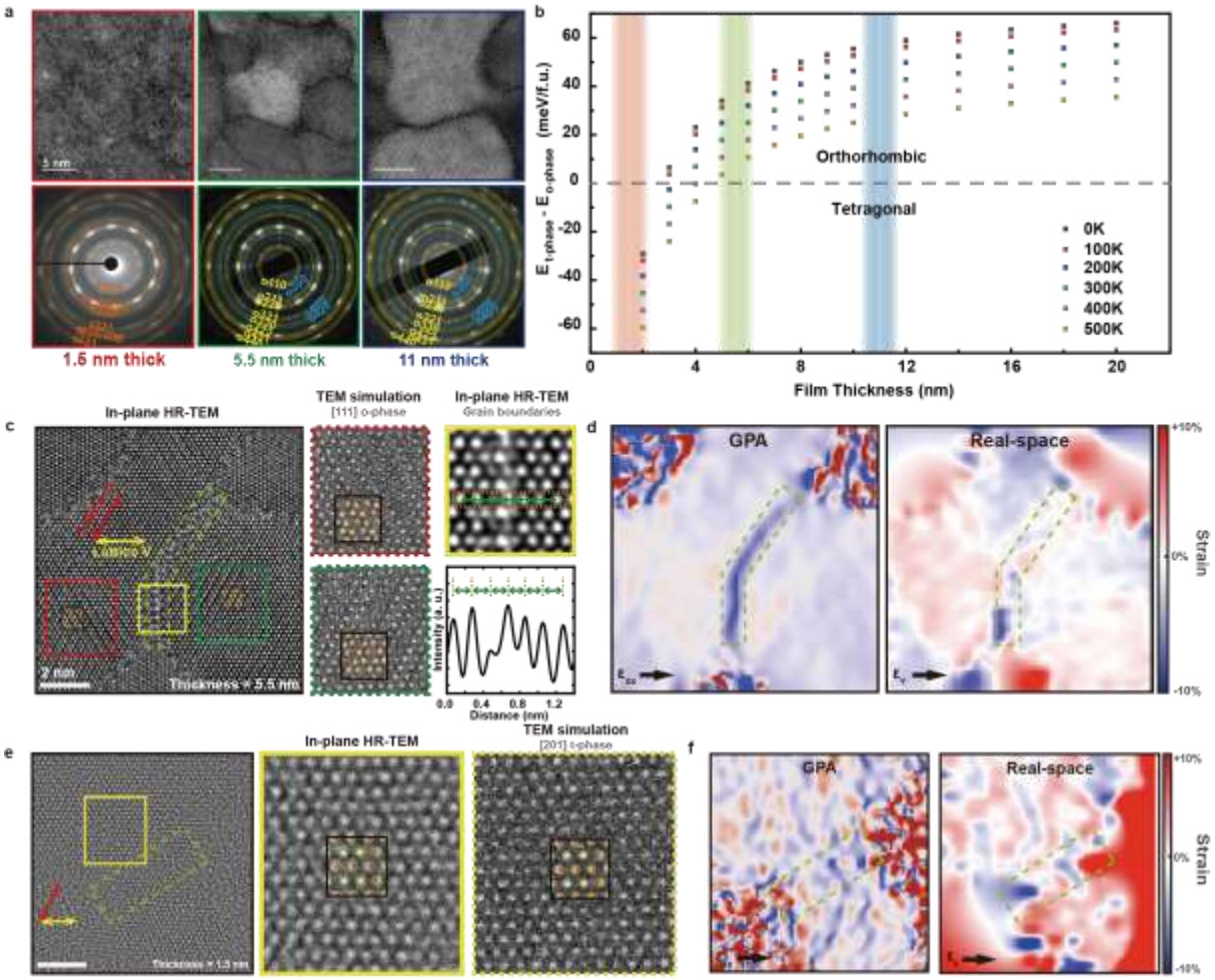

Figure 5. Atomic structure analysis of Y:HfO_2 thin films with varying thickness. (a) HR-TEM diffraction patterns of 1.5, 5.5, 11 nm thick films. (b) PTS using DFT regarding surface energy under various temperatures. (c) 5.5 nm-HfO_2 films HR-TEM images with the o-phase atomic model and simulation in [111] direction. (d) Corresponding strain maps from GPA and the real-space phase analysis. (e) 1.5 nm-HfO_2 film HR-TEM images with the t-phase atomic model and simulation in [201] direction. (f) Corresponding strain maps from GPA and the real-space phase analysis.

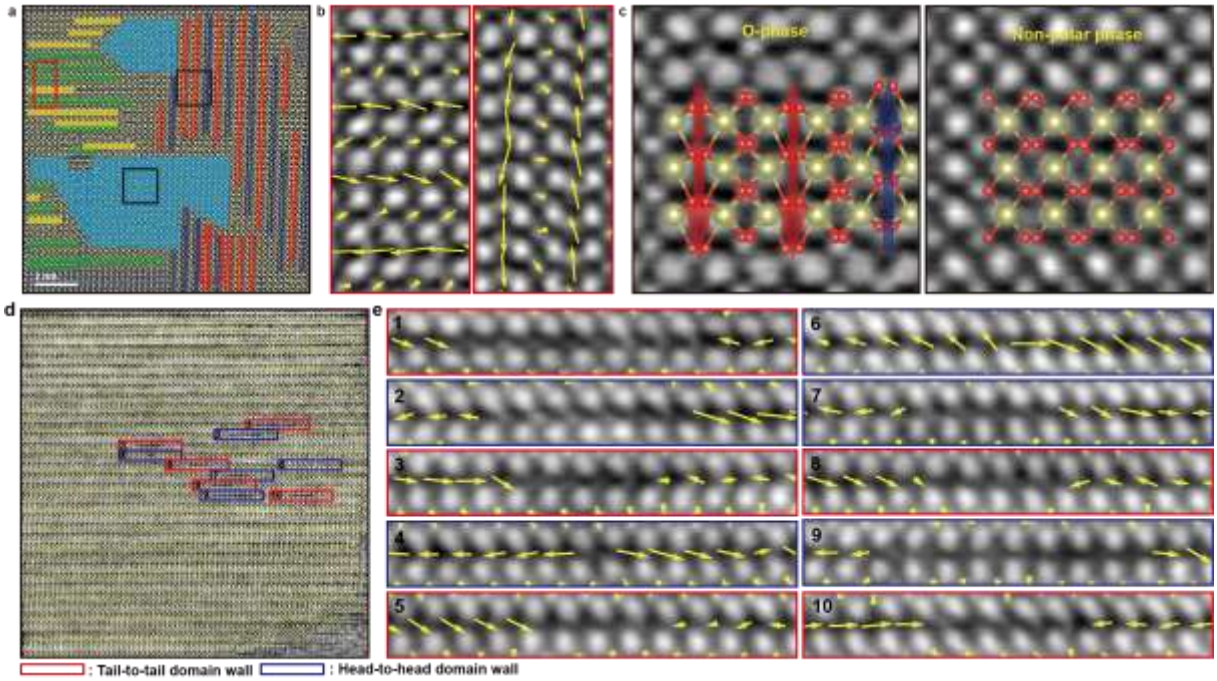

734

735 **Figure 6.** Observation of ferroelectric domain wall and arrangement using iDPC-STEM. (a)
736 iDPC-STEM images of the 5.5 nm-HfO_2 film. Yellow arrows overlaid on the iDPC-STEM
737 images indicate the displacement vectors of each oxygen atom. The lengths of arrows are
738 multiplied 5 times to visualize the directions. Red, blue, yellow, and green regions correspond
739 to downward, upward, rightward, and leftward displacement, respectively. The light blue
740 regions correspond to non-polar areas. (b) Enlarged images of regions marked with red boxes
741 in (a). (c) Enlarged images of black boxes show the atomic arrangement with models of the
742 polar phase and non-polar phase. (d) The domain map from the iDPC-STEM image. Red and
743 blue boxes represent the tail-to-tail and head-to-head domain walls, respectively. (e) Zoomed
744 images of the domain walls corresponding to the red and blue boxes in (d).

745

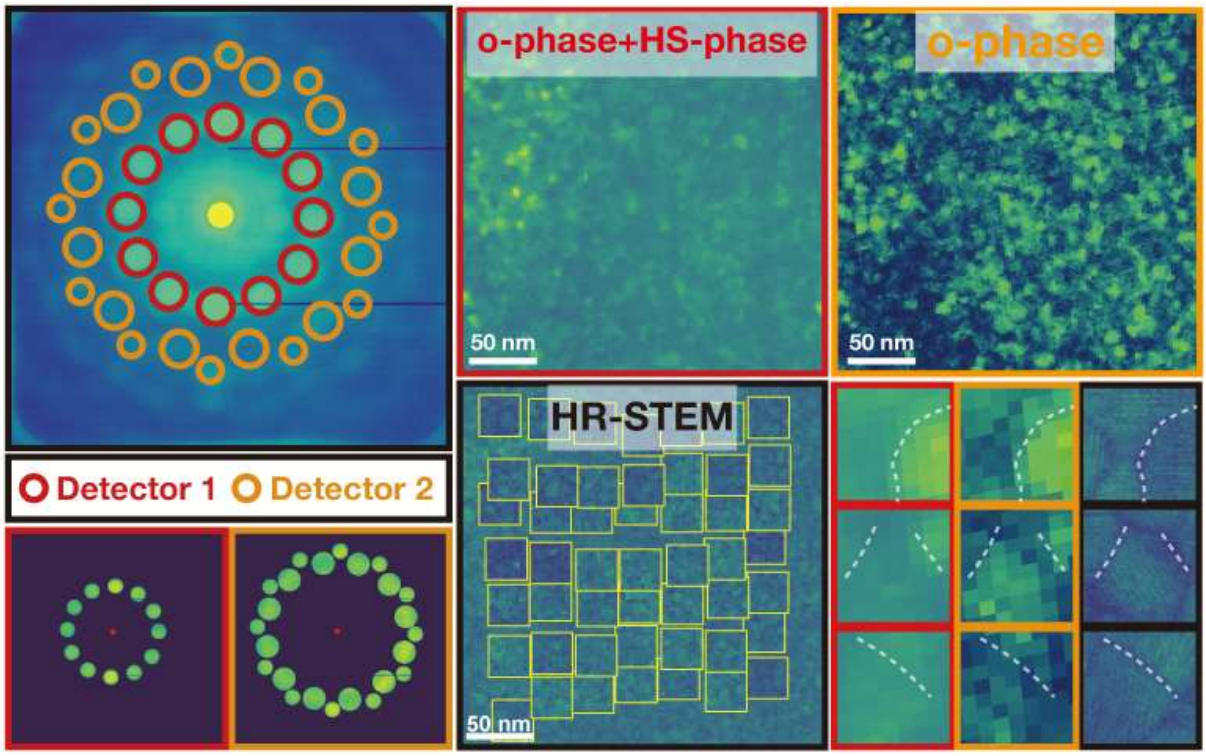
o-phase+HS-phase
50 nm
o-phase
50 nm
Detector 1
Detector 2
HR-STEM
50 nm

ToC graphic.